Journal of Biomedical Optics

BiomedicalOptics.SPIEDigitalLibrary.org

Self-guided reconstruction for time-domain fluorescence molecular lifetime tomography

Chuangjian Cai
Wenjuan Cai
Jiaju Cheng
Yuxuan Yang
Jianwen Luo

SPIE.

Chuangjian Cai, Wenjuan Cai, Jiaju Cheng, Yuxuan Yang, Jianwen Luo, "Self-guided reconstruction for time-domain fluorescence molecular lifetime tomography," *J. Biomed. Opt.* **21**(12), 126012 (2016), doi: 10.1117/1.JBO.21.12.126012.

Self-guided reconstruction for time-domain fluorescence molecular lifetime tomography

Chuangjian Cai,[a,†] Wenjuan Cai,[a,†] Jiaju Cheng,[a] Yuxuan Yang,[a] and Jianwen Luo[a,b,*]
[a]Tsinghua University, School of Medicine, Department of Biomedical Engineering, Beijing 100084, China
[b]Tsinghua University, Center for Biomedical Imaging Research, Beijing 100084, China

Abstract. Fluorescence probes have distinct yields and lifetimes when located in different environments, which makes the reconstruction of fluorescence molecular lifetime tomography (FMLT) challenging. To enhance the reconstruction performance of time-domain (TD) FMLT with heterogeneous targets, a self-guided L_1 regularization projected steepest descent (SGL1PSD) algorithm is proposed. Different from other algorithms performed in time domain, SGL1PSD introduces a time-resolved strategy into fluorescence yield reconstruction. The algorithm consists of four steps. Step 1 reconstructs the initial yield map with full time gate strategy; steps 2–4 reconstruct the inverse lifetime map, the yield map, and the inverse lifetime map again with time-resolved strategy, respectively. The reconstruction result of each step is used as *a priori* for the reconstruction of the next step. Projected iterated Tikhonov regularization algorithm is adopted for the yield map reconstructions in steps 1 and 3 to provide a solution with iterative refinement and nonnegative constraint. The inverse lifetime map reconstructions in steps 2 and 4 are based on L_1 regularization projected steepest descent algorithm, which employ the L_1 regularization to reduce the ill-posedness of the high-dimensional nonlinear problem. Phantom experiments with heterogeneous targets at different edge-to-edge distances demonstrate that SGL1PSD can provide high resolution and quantification accuracy for TD FMLT. [DOI: 10.1117/1.JBO.21.12.126012]

Keywords: fluorescence molecular lifetime tomography; time domain; L1 regularization; self-guided.

Paper 160632RR received Sep. 11, 2016; accepted for publication Nov. 30, 2016; published online Dec. 21, 2016.

1 Introduction

As a promising noninvasive molecular imaging modality, fluorescence molecular tomography (FMT) has been extensively explored for optical mammography, brain functional imaging, gene therapy, cancer diagnosis, and drug discovery.[1–4] With red-shifted and near-infrared fluorescent probes, FMT can realize macroscopical visualization and quantitative analysis of gene functions and protein expressions *in vivo*. According to the illumination source and the detector, FMT can be classified into the continuous wave (CW), frequency-domain (FD), and time-domain (TD) modes. The CW mode measures the steady fluorescent intensity passing through tissue with a charge-coupled device (CCD) detector for dense boundary sampling[5] and cannot realize the *in vivo* molecular lifetime measurement. The FD mode modulates the excitation light intensity at a single frequency and measures the intensity and phase signals at the same frequency with a heterodyne photomultiplier tube or a gain-modulation image-intensified CCD camera.[6,7] The TD mode uses an ultrashort pulse as the excitation light and measures the time-dependent fluorescent light with a time-gated intensified CCD camera[8,9] or a time-correlated single photon counting (TCSPC) system.[10] Both the FD and TD modes can be employed for fluorescence molecular lifetime tomography (FMLT), although the TD mode can provide information at all frequencies and, therefore, possess the richest information. Fluorescence molecular lifetime of fluorophores is sensitive to the physiological factors of the local environment, such as the concentration of tissue oxygenation and glucose and the pH of the tissue fluid.[11] Heterogeneous targets, opposite to homogeneous targets, mean that two targets employ different kinds of fluorescent molecules and solvents or have the different concentrations. Because molecular lifetime is sensitive to the physiological factors of the local environment, targets located in different environments have different characteristics. Heterogeneous targets make the FMLT reconstruction more difficult because the targets with larger molecular yields tend to restrain the reconstruction of the targets with smaller ones. Fluorescence molecular lifetime has been applied for the observation of fluorescence response energy transfer,[12] the reduction of the crosstalk between different fluorescent targets,[13] and the improvement of the resolution of fluorescence molecular yield tomography (FMYT).[14]

There are two main categories of methods for the reconstruction of FMLT. One is based on transforms, such as Fourier transform[15] and Laplace transform,[16] and the other turns the inverse problem into a linear one. Nothdurft et al. have suggested an algorithm with Fourier transform and an extension to the normalized Born approach and validated the robustness of this approach with *in vivo* experiments.[15] Gao et al. proposed the linear generalized pulse-spectrum technique (GPST) based on the Laplace-transformed coupled diffusion equations.[16,17] Compared with the Fourier transform scheme, the GPST is performed in the real domain and has improved noise robustness with appropriate transform factors to suppress the noise in the early and later parts of time-resolved curves. Although the transform scheme presents computational simplicity and redundancy reduction, it only utilizes a small part of the characteristic information and relies on the selection of the transform

*Address all correspondence to: Jianwen Luo, E-mail: luo_jianwen@tsinghua.edu.cn

†Contributed equally to this work.

1083-3668/2016/$25.00 © 2016 SPIE

factors. The other category of methods is directly performed in the time domain, i.e., adopting the time-resolved strategy. The time-resolved strategy can provide better quantification of the reconstruction and help set up a reliable reference for the evaluation of other methods and modes.[18–20] To simultaneously reconstruct the yield and lifetime, a Newton–Raphson scheme with an algebraic reconstruction technique (ART) to form the inner loops was proposed, and simulation experiments demonstrated the superiority of the time-resolved strategy to the transform scheme in the fidelity of image reconstruction.[20] However, simultaneous reconstruction of yield and lifetime turns to be a problem with severe ill-posedness. The L_1 regularization projected steepest descent (L1PSD) algorithm[18] and the accelerated nonlinear orthogonal matching pursuit (ANOMP) algorithm[19] previously proposed by our laboratory separate the reconstruction process into two parts, including the prereconstruction of the yield map with full time gate, which means that the whole emission light time curve is summed up, and the reconstruction of lifetime with time-resolved strategy. In this paper, phantom experiments demonstrate that both L1PSD and ANOMP obtain poor resolution for problems with heterogeneous targets mainly because of the information waste in full time strategy for the yield map reconstruction.

To better utilize the measurement data than previously proposed L1PSD and ANOMP, time-resolved strategy should also be adopted for the reconstruction of yield map. The time-resolved strategy for yield map reconstruction needs the lifetime *priori*, which also needs to be reconstructed. In this paper, a self-guided L_1 regularization projected steepest descent (SGL1PSD) algorithm is proposed. A self-guided algorithm means that the final lifetime reconstruction results are based on the lifetime reconstructed previously. The algorithm is divided into four steps. Step 1 reconstructs the yield map with full time gate strategy; steps 2–4 reconstruct the inverse lifetime map, the yield map, and the inverse lifetime map again with time-resolved strategy, respectively. The reconstruction result of each step is used as *a priori* for the reconstruction of the next step. The yield map reconstructions in steps 1 and 3 are based on the projected iterated Tikhonov regularization (PITK) algorithm, which can reduce the ill-posedness and provide a solution with iterative refinement and nonnegative constraint. The inverse lifetime map reconstructions in steps 2 and 4 are based on the L1PSD, which employs the L_1 regularization to reduce the ill-posedness of the high-dimensional nonlinear problem. The previously proposed L1PSD algorithm only consists of the reconstruction of a yield map with full time gate strategy and the reconstruction of a lifetime map with L1PSD, so the reconstruction of the yield map of L1PSD does not make good use of all the data. Different from L1PSD, SGL1PSD adds steps 3 and 4. In step 3, time-resolved reconstruction obtains a refinement of the yield map and is a better utilization of measurement data than step 1. The yield map regenerated in step 3 serves as the *priori* for the re-reconstruction of the inverse lifetime map in step 4, which is more accurate than the one reconstructed in step 2. The algorithm parameters of PITK in steps 1 and 3 can be the same, as are the algorithm parameters of L1PSD in steps 2 and 4. The stopping criteria of the four steps are all based on the difference of residual errors of iterations to ensure the convergence. Phantom experiments with targets at different edge-to-edge distances (EEDs) are performed to demonstrate that SGL1PSD can provide high resolution and quantification accuracy even when targets are heterogeneous.

2 Method

2.1 *Forward Model for Light Propagation*

The forward model for light propagation in tissue is adopted for the calculation of the distribution of the excitation light and the Green's function of the emission light, both on the temporal and spatial scales. The radiative transport equation (RTE) is regarded as the standard method for light modeling, but its direct solution has a high computational cost.[21] To overcome the limitations of RTE, spherical harmonic expansion is employed. Based on the first-order approximation of RTE, the telegraph equation (TE) is proposed for the calculation of the distribution of the excitation light[22]

$$\frac{D(r)}{c^2}\frac{\partial^2\Phi(r,t)}{\partial t^2}+\frac{1}{c}[3D(r)\mu_a(r)+1]\frac{\partial\Phi(r,t)}{\partial t}+\mu_a(r)\Phi(r,t)-\nabla\cdot[D(r)\nabla\Phi(r,t)]=S(r,t), \tag{1}$$

where $\Phi(r,t)$ is the photon density, $S(r,t)$ is the source term, c denotes the velocity of light, r denotes the spatial coordinate, t denotes the time, $\mu_a(r)$ denotes the absorption coefficient, and the diffusion coefficient $D(r)=1/\{3[\mu_a(r)+\mu_s'(r)]\}$, $\mu_s'(r)$ is the reduced scattering coefficient. Based on the fiber-coupled system, for the excitation light, the source term is defined as $S(r,t)=\delta(r-r_s)\delta(t)$, where r_s is the source position, and $S(r,t)$ is an isotropic impulse source. Robin-type boundary condition is employed[23]

$$\Phi(r,t)+2D(r)A\frac{\partial\Phi(r,t)}{\partial n}\bigg|_{r\in\partial\Omega}=0, \tag{2}$$

where A is related to the internal reflection coefficient at the air-tissue boundary.

Equation (1) is transformed with the standard Galerkin finite element method (Galerkin FEM), then the time derivatives are approximated with a finite difference scheme.[20,22] The temporal recursion matrix equation is obtained as

$$\left(\frac{M}{\Delta t^2}+\frac{D}{\Delta t}+K\right)\Phi(k+1)=\left(\frac{2M}{\Delta t^2}+\frac{D}{\Delta t}\right)\Phi(k)-\frac{M}{\Delta t^2}\Phi(k-1)+Q(k), \tag{3}$$

where k denotes the discrete time point, and Δt denotes the time interval. $\Phi(k)$ is the vector of light intensity on the FEM nodes and $\Phi(-1)=\Phi(0)=0$. M, D, and K are the matrices of $N_v\times N_v$, and $Q(k)$ is the vector of $N_v\times 1$, where N_v is the number of FEM nodes. The elements of M, D, K, and Q are given by

$$\begin{cases} M_{ij}=\int_\Omega\frac{D(r)}{c^2}u_i(r)u_j(r)\mathrm{d}\Omega \\ D_{ij}=\int_\Omega\frac{3D(r)\mu_a(r)+1}{c}u_i(r)u_j(r)\mathrm{d}\Omega \\ K_{ij}=\int_\Omega\mu_a(r)u_i(r)u_j(r)\mathrm{d}\Omega+\frac{1}{2A}\int_{\partial\Omega}u_i(r)u_j(r)\mathrm{d}(\partial\Omega), \\ \qquad\quad +\int_\Omega D(r)\nabla u_i(r)\cdot\nabla u_j(r)\mathrm{d}\Omega \\ Q_i(k)=\int_\Omega u_i(r)S(r,k)\mathrm{d}\Omega \end{cases} \tag{4}$$

where $u_i(r)$ and $u_j(r)$ are the shape functions at the nodes i and j, respectively.

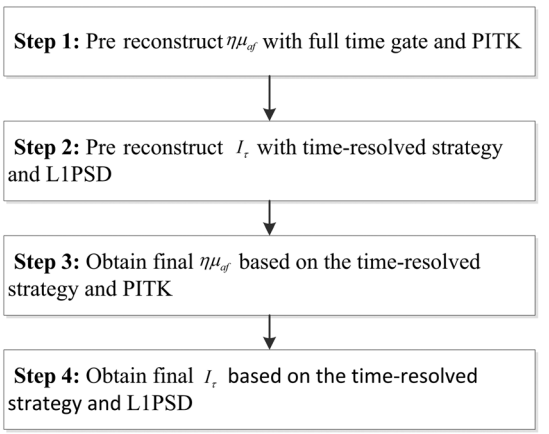

Fig. 1 Outline of the SGL1PSD. The reconstruction result of each step serves as a *priori* for the next step.

Through Eq. (3), the distribution of the excitation light $\Phi_x(r_s, r, t)$ can be obtained. When calculating $G_m(r, r_d, t)$, where r_d is the emission signal detection point, the adjoint method is adopted to reduce the computational cost,[23] so the source term $S(r, t)$ and the boundary condition are given by

$$\begin{cases} S(r,t) = 0 \\ \Phi(r,t) + 2D(r)A\frac{\partial\Phi(r,t)}{\partial n} = \delta(r - r_d)\delta(t), \ r \in \partial\Omega \end{cases}. \tag{5}$$

2.2 *Inverse Model*

The emission signal $\Phi_m(r_s, r_d, t)$ detected at r_d, for an excitation source at r_s, and the fluorophore distribution $E(r, t)$ can be formulated as

$$\begin{cases} \Phi_m(r_s, r_d, t) = \int_\Omega \Phi_x(r_s, r, t) * G_m(r, r_d, t) * E(r, t)\mathrm{d}^3 r \\ E(r,t) = \eta\mu_{af}(r)\exp[-t/\tau(r)]/\tau(r)u(t) \end{cases}, \tag{6}$$

where $u(t)$ denotes the unit step function, $\eta\mu_{af}(r)$ denotes the fluorescence yield, and $\tau(r)$ denotes the fluorescence lifetime. To avoid dealing with the singularity of the zero points, the inverse lifetime is defined as $I_\tau(r) = 1/\tau(r)$, so the fluorophore distribution turns to be $E(r,t) = \eta\mu_{af}(r)I_\tau(r)\exp[-I_\tau(r)t]u(t)$. In the background, $I_\tau(r)$ is assumed to be 0, so $E(r, t) = 0$ for the background.

2.2.1 *Self-guided L1 regularization projected steepest descent algorithm*

To better utilize the data collected, the SGL1PSD algorithm is proposed. The outline of SGL1PSD is shown in Fig. 1. The final lifetime tomography image is obtained according to the reconstructed inverse lifetime map I_τ in step 4. The previously proposed L1PSD algorithm only consists of the reconstruction of the yield map with full-time gate strategy and the reconstruction of an inverse lifetime map with L1PSD, so the reconstruction of the yield map in L1PSD does not make good use of all the data. Different from L1PSD, SGL1PSD adds steps 3 to 4. In step 3, the yield map $\eta\mu_{\mathrm{af}}$ is regenerated based on the time-resolved reconstruction strategy, which can serve as the *priori* for the re-reconstruction of the inverse lifetime map I_τ in step 4. To reconstruct the yield map $\eta\mu_{af}$ in steps 1 and 3, PITK is proposed.

2.2.2 *Projected iterated Tikhonov regularization method for yield map reconstruction*

For matrix equation $WX = b$, where W is a matrix of $N_1 \times N_2$, b is a vector of $N_1 \times 1$, and X is the vector to be solved, the iterated Tikhonov regularization method[24] can be adopted to obtain a solution with iterative refinement. If $N_1 \le N_2$, the iterative equation is

$$X_{k+1} = X_k - W^{\mathrm{T}}[WW^{\mathrm{T}} + \alpha \times \mathrm{tr}(WW^{\mathrm{T}})I]^{-1}(WX_k - b), \tag{7}$$

where α is the regularization parameter, $\mathrm{tr}(\cdot)$ denotes the operator that obtains the trace of a matrix, and T denotes the matrix transposition operator.

If $N_1 > N_2$, to reduce the computational complexity, Eq. (7) can be transformed to the following form:

$$X_{k+1} = X_k - [W^{\mathrm{T}}W + \alpha \times \mathrm{tr}(W^{\mathrm{T}}W)I]^{-1}W^{\mathrm{T}}(WX_k - b). \tag{8}$$

To satisfy the nonnegative constraint of FMYT, the projection strategy is adopted. The stopping criterion is based on the residual errors. To reduce the computational cost, the termination judgment is carried out every 50 iterations. The stopping criterion is $|\Delta R_{\eta\mu_{af}}|/R^1_{\eta\mu_{af}} < \xi_{\eta\mu_{af}}$, where $\xi_{\eta\mu_{af}}$ denotes the maximum ratio between the difference of the residual errors and the initial residual error, the initial residual error $R^1_{\eta\mu_{af}} = \|WX_{50} - b\|_2$ and the difference of residual errors $\Delta R_{\eta\mu_{af}} = \|WX_{50\times(l+1)} - b\|_2 - \|WX_{50\times l} - b\|_2$, where l is an integer. The PITK algorithm is summarized in Fig. 2 in which % is the modulus operator.

In step 1, with the image domain discretized into N_{G} voxels, the matrix equation to be solved is

$$W_{\eta\mu_{af}}\eta\mu_{af} = R_{\Phi_m}, \tag{9}$$

where $W_{\eta\mu_{af}}$ denotes the weight matrix mapping the yield map into the rearranged measurement emitted light R_{Φ_m} with the full time gate strategy. $\eta\mu_{af}$, $W_{\eta\mu_{af}}$, and R_{Φ_m} are expressed as

$$\begin{cases} \eta\mu_{af} = [\eta\mu_{af}(r_1) \quad \eta\mu_{af}(r_2) \quad \dots \quad \eta\mu_{af}(r_{N_G})]^T \\ W_{\eta\mu_{af}} = \begin{pmatrix} \mathrm{W}^{\eta\mu_{af}}_{11} & \dots & \mathrm{W}^{\eta\mu_{af}}_{1N_G} \\ \vdots & \ddots & \vdots \\ \mathrm{W}^{\eta\mu_{af}}_{(S\times D)1} & \dots & \mathrm{W}^{\eta\mu_{af}}_{(S\times D)N_G} \end{pmatrix} \\ \mathrm{W}^{\eta\mu_{af}}_{ij} = \Delta V \int_{t=o}^{T_{\mathrm{gate}}} \Phi_x(r_s^{F_i}, r_j, t) * G_m(r_j, r_d^{F_i}, t)\mathrm{d}t \\ R_{\Phi_m} = \left[\int_{t=0}^{T_{\mathrm{gate}}} \Phi_m(r_s^{F_1}, r_d^{F_1}, t)\mathrm{d}t \int_{t=0}^{T_{\mathrm{gate}}} \Phi_m(r_s^{F_2}, r_d^{F_2}, t)\mathrm{d}t \dots \int_{t=0}^{T_{\mathrm{gate}}} \Phi_m(r_s^{F_{S\times D}}, r_d^{F_{S\times D}}, t)\mathrm{d}t\right]^T \end{cases}, \tag{10}$$

where T_{gate} denotes the full time gate, S denotes the number of excitation sources, D denotes the number of detectors, and ΔV denotes the voxel volume.

where $A_{\eta\mu_{af}}$ and Φ_m are expressed as

$$\begin{cases} A_{\eta\mu_{af}} = \begin{pmatrix} \mathrm{A}_{11}^{\eta\mu_{af}} & \cdots & \mathrm{A}_{1N_G}^{\eta\mu_{af}} \\ \vdots & \ddots & \vdots \\ \mathrm{A}_{(S\times D\times I)1}^{\eta\mu_{af}} & \cdots & \mathrm{A}_{(S\times D\times I)N_G}^{\eta\mu_{af}} \end{pmatrix}, \\ \Phi_m = [\Phi_m(r_s^1, r_d^1, t)|_{t=t^1}\ \Phi_m(r_s^2, r_d^2, t)|_{t=t^2} \ldots \Phi_m(r_s^{S\times D\times I}, r_d^{S\times D\times I}, t)|_{t=t^{S\times D\times I}}] \end{cases}$$

$$A_{ij}^{\eta\mu_{af}} = \Delta V\{\Phi_x(r_s^i, r_j, t)* G_m(r_j, r_d^i, t) * [I_\tau(r_j)e^{-I_\tau(r_j)t}u(t)]\}|_{t=t^i}\ , \tag{12}$$

where I is the number of discretized time points.

According to Eq. (11), the reconstruction of the yield map in step 3 is based on time-resolved strategy, which can better utilize the measurement data than Eq. (9) and realize the accurate reconstruction of the yield map.

2.2.3 *L1 regularization projected steepest descent algorithm for inverse lifetime map reconstruction*

The L1PSD algorithm[18] is adopted for the reconstruction of an inverse lifetime map in steps 2 and 4. The fluorophore distribution $E(r,t)$ has been adjusted slightly, with the light speed term removed to simplify the equations, as compared with the previous paper.[18] The objective equation for the inverse lifetime map is nonlinear and can be formulated as

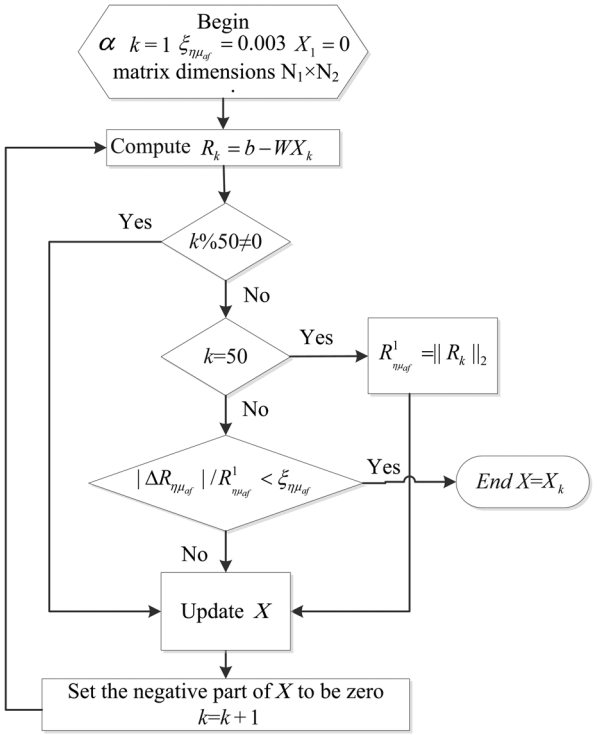

Fig. 2 Flow chart of PITK algorithm. α denotes the regularization parameter, $\xi_{\eta\mu_{af}}$ denotes the maximum ratio between the difference of residual errors and the initial residual error, k denotes the iteration number, X denotes the vector to be solved, and R_k is the residual error.

In step 3, the matrix equation to be solved is

$$A_{\eta\mu_{af}}\eta\mu_{af} = \Phi_m, \tag{11}$$

$$\Phi_m = F(I_\tau), \tag{13}$$

where Φ_m is defined in Eq. (12), and the elements of $F(I_\tau)$ are

$$\begin{aligned} F^i &= \sum_{n=1}^{N_G} F_n^i \Delta V \\ &= \sum_{n=1}^{N_G} \Delta V\{\Phi_x(r_s^i, r_n, t) * G_m(r_n, r_d^i, t) \\ &\quad * [\eta\mu_{af}(r_n)I_\tau(r_n)e^{-I_\tau(r_n)t}u(t)]\}|_{t=t^i}. \end{aligned} \tag{14}$$

As compared with Ref. 18, the equation of the element of gradient of F is also adjusted slightly,

$$\begin{aligned} \nabla F_n^i &= \Delta V(\Phi_x(r_s^i, r_n, t) * G_m(r_n, r_d^i, t) \\ &\quad * \{\eta\mu_{af}(r_n)[1 - I_\tau(r_n)t]\mathrm{e}^{-I_\tau(r_n)t}u(t)\})|_{t=t^i}. \end{aligned} \tag{15}$$

To guarantee the uniqueness, L_1 regularization is adopted, so the optimization function is developed as

$$\min_{I_\tau \geq 0}\left\{\frac{1}{2}\left[\|F(I_\tau) - \Phi_m\|_2^2 + \lambda\sqrt{\|I_\tau\|_2^2 + \mu}\right]\right\}, \tag{16}$$

where μ is a positive smooth parameter for preventing instability from the differentiation and λ is the regularization parameter. The initial value of the inverse lifetime is set to be 10^8 s^{-1}, the initial regularization parameter is set to be 1.2×10^{-14}, the attenuation coefficient of the regularization parameter $D_e = 0.6$, and the smooth parameter $\mu = 10^8$.

To reduce the computational cost, in steps 2 to 4, only the elements with nonzero values in the reconstruction results of the previous step are taken into account. The algorithm parameters of PITK in steps 1 and 3 can be the same, as are the algorithm parameters of L1PSD in steps 2 and 4. For the regularization parameter of PITK, the empirical range is 0.01 to 0.5. For the maximum ratio of the difference of the residual errors of adjacent iterations and the initial residual error ξ_{I_τ} of L1PSD, more accurate results can be obtained with smaller ξ_{I_τ}, but at the cost of an increased computational cost. The suitable range of ξ_{I_τ} is 0.00005 to 0.0005.

2.3 *Quantitative Metrics for Fluorescence Molecular Lifetime Tomography Reconstruction*

The valley lifetime value of a reconstructed target could be selected as the reconstruction value.[18] The absolute error (AE) of a reconstructed target is defined

$$\mathrm{AE} = |\tau_{\mathrm{recon}} - \tau_{\mathrm{real}}|, \tag{17}$$

where τ_{recon} and τ_{real} denote the reconstruction value and the real lifetime value. For a phantom with two targets, $\mathrm{AE}_{\mathrm{max}}$ represents the larger one of the AEs of two reconstructed targets.

To provide the overall quantification accuracy, the root-mean-square error (RMSE) of inverse lifetime reconstruction is calculated as

$$\mathrm{RMSE} = \sqrt{\left[\sum_{i=1}^{\mathrm{num}} (I_{\tau,i}^{\mathrm{recon}} - I_{\tau,i}^{\mathrm{real}})^2\right] / \mathrm{num}}, \tag{18}$$

where $I_{\tau,i}^{\mathrm{recon}}$ and $I_{\tau,i}^{\mathrm{real}}$ are the reconstructed inverse lifetime and real inverse lifetime of the ith element, respectively, and num is the number of elements to be evaluated.

The separability is introduced to evaluate the resolution. If two targets are separated thoroughly in the inverse lifetime tomographic image, the targets are considered to be separable. Because the lifetime value is the reciprocal of the inverse lifetime value, the separability of the inverse lifetime tomographic image also reflects the resolution of the lifetime image.

3 Experiments and Results

3.1 *Materials and Methods*

To evaluate the performance of SGL1PSD, three phantom experiments, i.e., Experiments 1, 2, and 3, with heterogeneous targets at different EEDs (6, 3, and 1.5 mm, respectively), were carried out. The phantom experiments were based on the fiber-coupled, time-correlated and TCSPC system previously established by our laboratory.[18,19] The wavelength of the ultrashort point incident light was slightly changed to 780 nm, while the center wavelength of the filter group was still 840 nm. The measurement parameters, i.e., the number of projections S, number of detection points D for each projection, and the number of effective time points I, were the same as those in Ref. 19. The measurement data were normalized by the summation of all the measurement data to eliminate the effects of source power, efficiency of fibers and filter group, and magnification of the detector. The phantom size, tube size, and component of the background were the same as those in Ref. 19, while the components of the targets were set to be heterogeneous to test the algorithm performance. One cylinder was filled with 10-μM indocyanine green/dimethyl *sulfoxide* (ICG/DMSO), the other was filled with 10-μM ICG/absolute alcohol (ICG/ALC). The molecular lifetimes of ICG/DMSO and ICG/ALC were 0.97 and 0.62 ns, respectively.[25] The optical parameters of 1% intralipid solution at the excitation and emission wavelengths were set according to Ref. 26.

In the reconstruction, the geometry model was discretized into 16,989 nodes and 91,985 tetrahedral elements. With Galerkin FEM,[20,22] the distributions of excitation light and Green's function of the emission light were calculated. The target domain only took into account the region containing fluorophores. Thus the target domain was 30 mm in diameter and 10 mm in height. The target domain was discretized into 11,646 voxels of size $0.6 \times 0.6 \times 2$ mm^3. The distributions of excitation light $\Phi_x(r_s, r_n, t)$ and Green's function of emission light $G_m(r_n, r_d, t)$ were interpolated. $\Phi_x(r_s^i, r_n, t) * G_m(r_n, r_d^i, t)|_{t=t^i}$ $(i = 1, 2, \ldots, S \times D \times I, n = 1, 2, \ldots, N_G)$ in Eq. (6) was normalized by the maximum value.

3.2 *Results*

To better illustrate the principle of SGL1PSD, the step-by-step results of Experiment 1 are shown in Fig. 3. With the reconstruction parameters, the nonzero region of the reconstructed yield map of step 1 is relatively large. Because the reconstruction in step 2 is based on the reconstructed yield map in step 1, the intermediate inverse lifetime map in step 2 also has a wide distribution, which can ensure that the region of the targets is included and provides a better *priori* for steps 3 and 4. Given the reconstructed inverse lifetime map in step 2, the yield map can be regenerated with time-resolved strategy, according to Eq. (11), which can better utilize the measurement data than a full time gate strategy. Therefore, the regenerated inverse lifetime map in step 4 can provide high resolution and quantification accuracy.

Figures 4–6 are the final reconstruction results of the three phantom experiments (i.e., Experiments 1, 2, and 3, respectively). The corresponding results of the L1PSD and the ANOMP algorithm are also presented for comparison. The ANOMP algorithm is based on the greedy strategy to enhance the reconstruction resolution, which performs well for homogeneous targets. Figures 4(a)–4(c), 5(a)–5(c), and 6(a)–6(c) are the reconstructed inverse lifetime tomographic images of SGL1PSD, L1PSD, and ANOMP of Experiments 1, 2, and 3, respectively. Figures 4(d), 5(d), and 6(d) are the inverse lifetime profiles along the dotted lines indicated in the inverse lifetime tomographic images. Figures 4(e)–4(h), 5(e)–5(h), and 6(e)–6(h) are the corresponding lifetime results. Because the small values of inverse lifetime in the background turn into large values of lifetime, the values exceeding 2 ns are eliminated in the lifetime tomographic images.

When the EED is not too small (Experiment 1, EED = 6 mm), the two reconstructed targets of all the three reconstruction algorithms [Figs. 4(a)–4(c)] can be separated. Due to the heterogeneous characteristic of targets, the reconstruction is difficult. The real sizes of the two targets are the same. However, the ICG/DMSO solution has a higher fluorescence molecular yield (FMY), so it is difficult to keep the same size of the targets in FMYT with only the full time gate. The yield *priori* of the L1PSD and ANOMP algorithms is generated based on the full time gate strategy. Step 3 of SGL1PSD is based on the time-resolved strategy and can better utilize measurement data than the full time gate strategy, so the FMYT in step 3 of SGL1PSD can obtain a more accurate FMY distribution. As can be seen in Figs. 4(a)–4(c), the shapes of the reconstructed targets of SGL1PSD are closer to the real shapes. Figure 4(d) demonstrates that the inverse lifetime profile of SGL1PSD is also closer to the real distribution. For the quantification accuracy of the ICG/DMSO solution, SGL1PSD performs better than L1PSD and ANOMP.

In Experiment 2, where the EED is 3 mm, only the reconstructed targets of SGL1PSD [Fig. 5(a)] are separated. The reconstructed targets of L1PSD are bound together. For ANOMP, if the support set covers the distribution of the ICG/DMSO target, the iterations reach a local optimum and more iterations do not improve the reconstruction resolution.

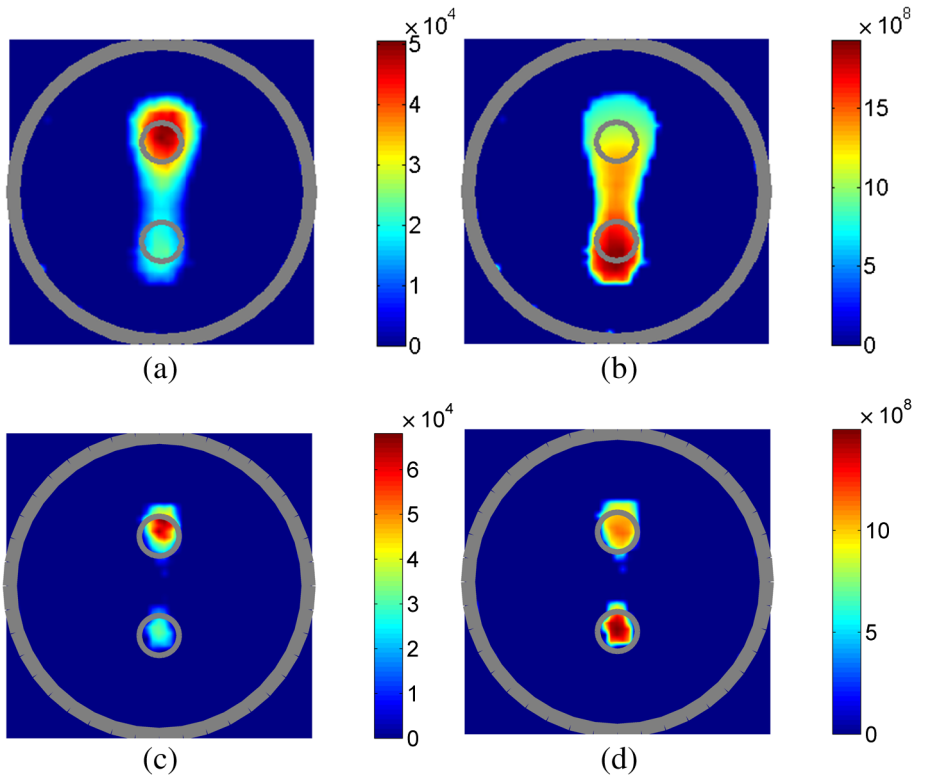

Fig. 3 Results of Experiment 1 in each step of SGL1PSD. (a) The reconstructed yield map in step 1. (b) The reconstructed inverse lifetime map in step 2 (unit: s^{-1}). (c) The regenerated yield map in step 3. (d) The regenerated inverse lifetime map in step 4 (unit: s^{-1}).

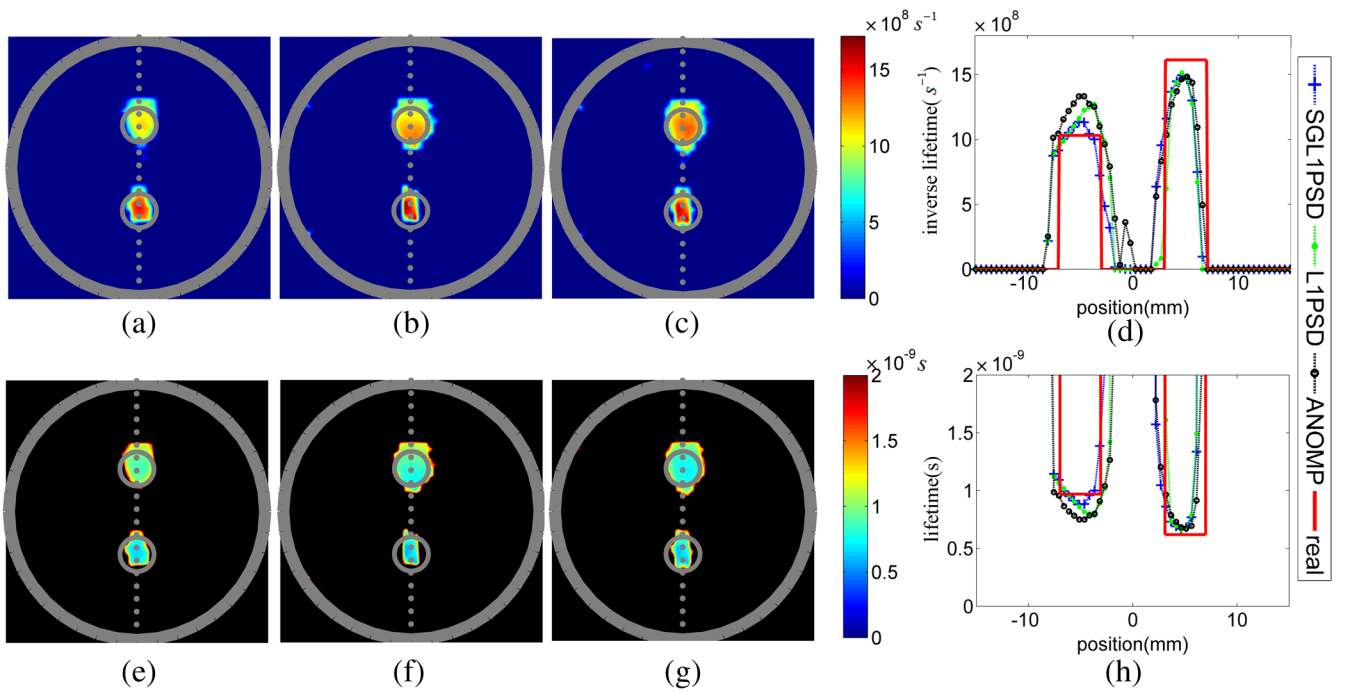

Fig. 4 The reconstruction results of Experiment 1 (EED = 6 mm). (a), (b), and (c) are the reconstructed inverse lifetime tomographic images of SGL1PSD, L1PSD, and ANOMP (unit: s^{-1}), respectively. (d) shows the inverse lifetime profiles along the dotted lines indicated in (a), (b), and (c). Horizontal and vertical axes denote location (unit: mm) and inverse lifetime (unit: s^{-1}), respectively. (e), (f), and (g) are the corresponding lifetime tomographic images of SGL1PSD, L1PSD, and ANOMP (unit: s). The lifetimes exceeding 2 ns are marked with black color. (h) shows the lifetime profiles along the dotted lines indicated in (e), (f), and (g). Horizontal and vertical axes denote location (unit: mm) and lifetime (unit: s), respectively. In (d) and (h), the blue, green, and black lines correspond to the results of SGL1PSD, L1PSD, and ANOMP, and red line shows the real values.

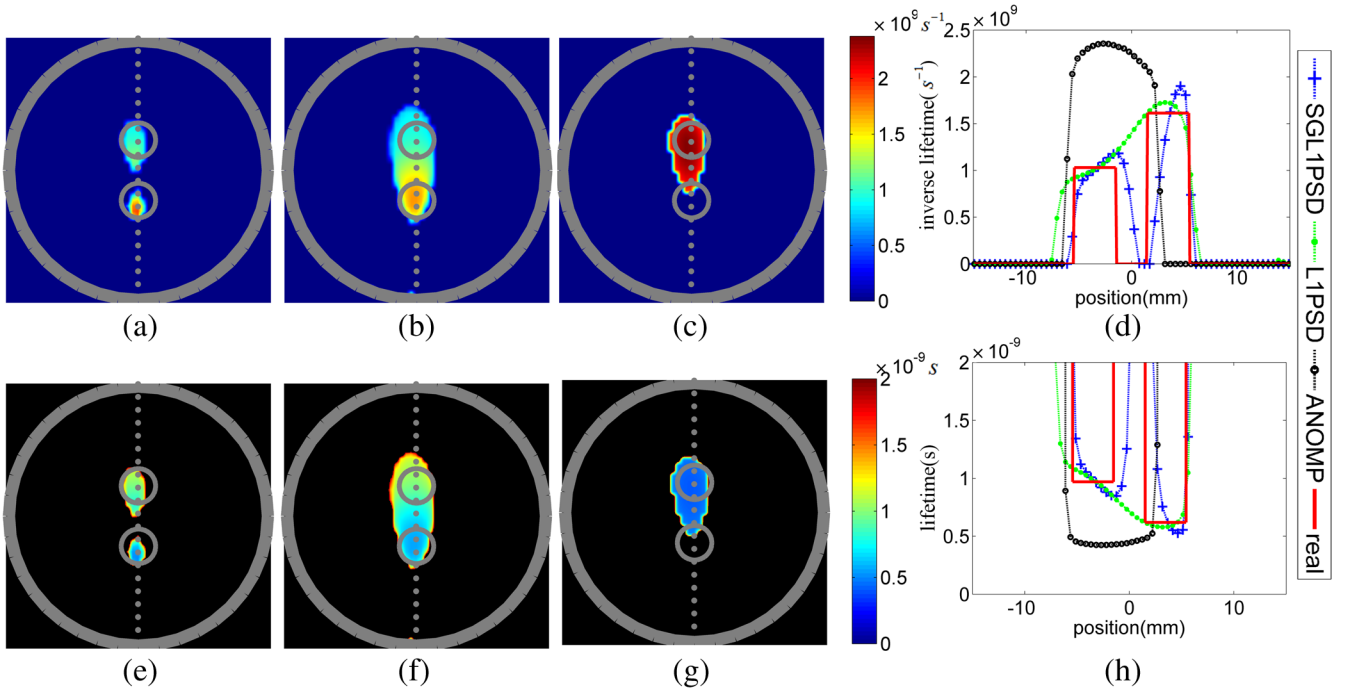

Fig. 5 The reconstruction results of Experiment 2 (EED = 3 mm). (a), (b), and (c) are the reconstructed inverse lifetime tomographic images of SGL1PSD, L1PSD, and ANOMP (unit: s^{-1}). (d) shows the inverse lifetime profiles along the dotted lines indicated in (a), (b), and (c). Horizontal and vertical axes denote location (unit: mm) and inverse lifetime (unit: s^{-1}), respectively. (e), (f), and (g) are the corresponding lifetime tomographic images of SGL1PSD, L1PSD, and ANOMP (unit: s). The lifetimes exceeding 2 ns are marked with black color. (h) shows the lifetime profiles along the dotted lines indicated in (e), (f), and (g). Horizontal and vertical axes denote location (unit: mm) and lifetime (unit: s), respectively. In (d) and (h), the blue, green, and black lines correspond to the results of SGL1PSD, L1PSD, and ANOMP, and red line shows the real values.

The profiles in Figs. 5(d) and 5(h) demonstrate that the reconstruction values of SGL1PSD are close to the real values.

In Experiment 3, the EED is only 1.5 mm. The reconstructed targets of SGL1PSD can still be separated [Fig. 6(a)], whereas the results of L1PSD and ANOMP [Figs. 6(b) and 6(c)] are still inseparable. The reconstruction values of SGL1PSD remain accurate [Figs. 6(d) and 6(h)]. However, although SGL1PSD provides high resolution, the reconstructed targets in Fig. 6(a) are small.

Table 1 summarizes the evaluation metrics of the reconstruction results. When two reconstructed targets cannot be separated, the AE_{max} is not available (NA). For Experiment 1, the AE_{max} of SGL1PSD is much smaller than those of L1PSD and ANOMP. For Experiments 2 and 3, the AE_{max}s of SGL1PSD remain small, whereas those of L1PSD and ANOMP are NA. The RMSE can evaluate the overall reconstruction accuracy of the inverse lifetime. When EED = 6 mm, the RMSEs of the three algorithms are close and relatively small. However, when the heterogeneous targets are close (EED = 3 or 1.5 mm), the reconstruction results of ANOMP are inaccurate and the RMSEs are obviously larger than those of SGL1PSD and L1PSD. When the EEDs are small (EED = 3 or 1.5 mm), the reconstructed targets of SGL1PSD are still separable, whereas those of L1PSD and ANOMP cannot be separated. The runtimes of different experiments and algorithms are also summarized in Table 1. The runtimes of SGL1PSD are slightly longer than those of L1PSD. For Experiment 1, the runtime of ANOMP is much longer than the others. However, in Experiments 2 and 3, the runtimes of ANOMP are relatively short. In Experiments 2 and 3, the inner iterations of ANOMP are unstable and the residual error sometimes increases, which makes the inner iterations terminate too early; so the runtimes are not long. The results of ANOMP in Experiments 2 and 3 are inaccurate, so the runtimes of ANOMP in Experiments 2 and 3 are meaningless. Further experiments show that the minimum distances of heterogeneous targets that SGL1PSD, L1PSD, and ANOMP can resolve are 1.5, 5, and 5 mm, as summarized in Table 2.

4 Discussion

Fluorescence molecular lifetime of fluorophores depends on the physiological factors of the local environment. It can be used to observe fluorescence response energy transfer, to reduce the crosstalk between different fluorescent targets, and to improve the resolution of FMYT.[11–14] The reconstruction methods of FMLT directly based on the time strategy, including L1PSD and ANOMP, do not utilize all the information when reconstructing the FMY *priori*. To better utilize the measurement data, the SGL1PSD algorithm is proposed. SGL1PSD introduces a time-resolved strategy for the reconstruction of a molecular yield map to provide more accurate *priori* for lifetime reconstruction. Because the time-resolved reconstruction of the yield map also has to use the *priori* of the lifetime map, extra reconstruction steps are needed. The SGL1PSD algorithm can be divided into four steps and reconstructs the yield map and inverse lifetime map alternatively. The previous methods, i.e., L1PSD and ANOMP, only utilize the full time gate strategy to reconstruct the yield. The full time gate means that the whole

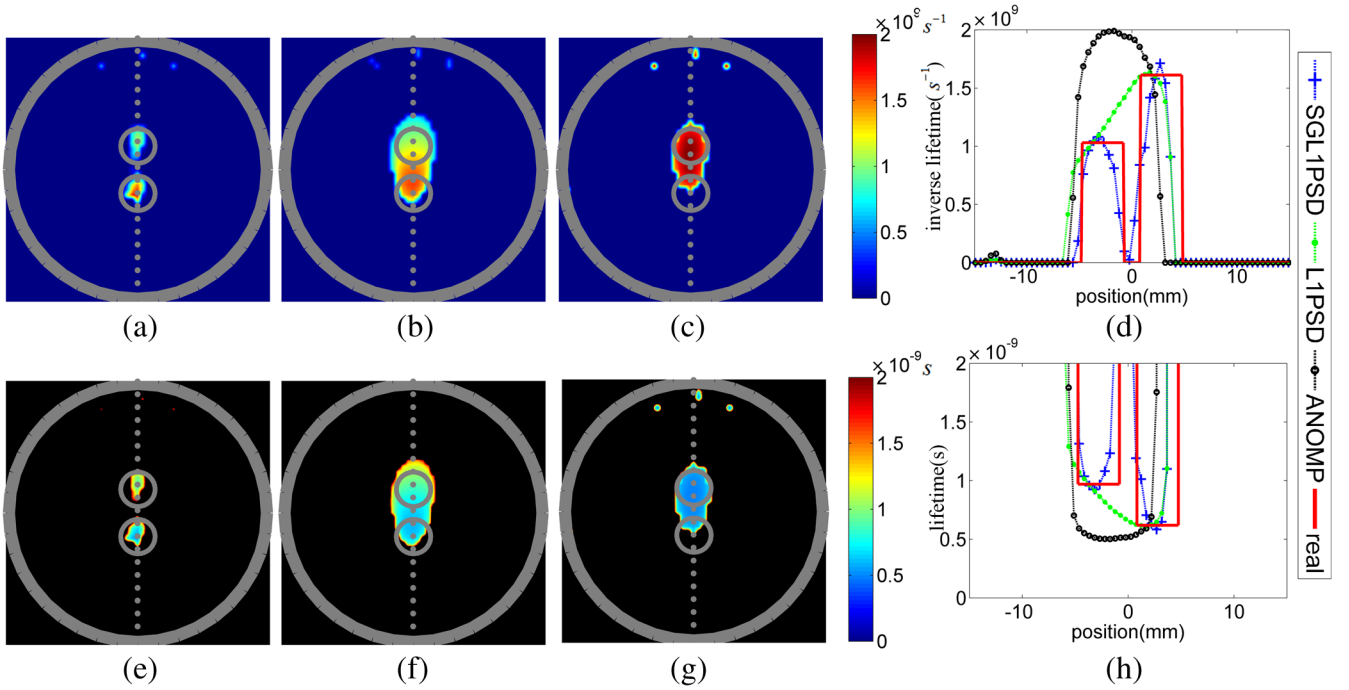

Fig. 6 The reconstruction results of Experiment 3 (EED = 1.5 mm). (a), (b), and (c) are the reconstructed inverse lifetime tomographic images of SGL1PSD, L1PSD, and ANOMP (unit: s^{-1}). (d) shows the inverse lifetime profiles along the dotted lines indicated in (a), (b), and (c). Horizontal and vertical axes denote location (unit: mm) and inverse lifetime (unit: s^{-1}), respectively. (e), (f), and (g) are the corresponding lifetime tomographic images of SGL1PSD, L1PSD, and ANOMP (unit: s). The lifetimes exceeding 2 ns are marked with black color. (h) shows the lifetime profiles along the dotted lines indicated in (e), (f), and (g). Horizontal and vertical axes denote location (unit: mm) and lifetime (unit: s), respectively. In (d) and (h), the blue, green, and black lines correspond to the results of SGL1PSD, L1PSD, and ANOMP, and red line shows the real values.

Table 1 Quantitative metrics of reconstruction results.

Experiment	EED (mm)	Algorithm	AE_{max} (ns)	RMSE (10^9 s^{-1})	Separable	Runtime (s)
1	6	SGL1PSD	0.11	0.18	Yes	513
		L1PSD	0.21	0.22	Yes	427
		ANOMP	0.24	0.21	Yes	1039
2	3	SGL1PSD	0.14	0.21	Yes	661
		L1PSD	NA	0.25	No	530
		ANOMP	NA	0.41	No	366
3	1.5	SGL1PSD	0.08	0.21	Yes	580
		L1PSD	NA	0.24	No	450
		ANOMP	NA	0.32	No	256

Note: NA: not available.

Table 2 Minimum distances of heterogeneous targets that can be resolved.

	SGL1PSD	L1PSD	ANOMP
Minimum distance (mm)	1.5	5	5

emission light time curve is summed up and only the total strength of the whole time curves is taken into account. In SGL1PSD, step 3 adopts the time-resolved strategy for yield reconstruction and directly takes into account the discrete time points of time curves. The time-resolved strategy can utilize the information of temporal changes, not just the total strength of the time curves. The reconstruction problems of the yield map in steps 1 and 3 are linear, and the PITK algorithm is adopted to reduce the ill-posedness. The PITK algorithm adds a nonnegative constraint to the iterated Tikhonov regularization algorithm, which can provide a nonnegative solution with iterative refinement. Two equivalent iterative equations are presented for PITK to reduce the computational cost according to the matrix dimensions. The stopping criterion is based on the difference of residual errors of iterations to ensure the convergence. To reduce the computational cost, the termination judgment is carried out every 50 iterations. The inverse lifetime map reconstructions in steps 2 and 4 are based on the L1PSD, which employs the L_1 regularization to reduce the ill-posedness of the high-dimensional nonlinear problem. The analytical equations of the search direction and step are given. The regularization parameter is decreased after each iteration to accelerate the convergence. The stopping criterion is based on the difference of the residual errors of adjacent iterations to ensure the convergence. The time-resolved reconstruction of the yield map in step 3 is the key part of SGL1PSD, which is a refinement of the yield map and a better utilization of measurement data than step 1. The re-reconstructed inverse lifetime map in step 4 is

based on the regenerated yield map in step 3, so the final result is accurate. The algorithm parameters of PITK in steps 1 and 3 can be the same, as are the algorithm parameters of L1PSD in steps 2 and 4. The support set method is employed to reduce the computation cost of SGL1PSD. In steps 2 to 4, only the elements with nonzero values in the reconstruction results of the previous step are taken into account. Compared with the equations used before,[18,19] the basic equation of fluorophore distribution is adjusted slightly, with the light speed term dropped.

To evaluate the performance of the SGL1PSD, three phantom experiments with heterogeneous targets, i.e., the target of ICG/DMSO and the target of ICG/ALC, at different EEDs (6, 3, and 1.5 mm, respectively) were carried out. As for the phantom setup, 1% intralipid has absorption and a strong scattering effect for light, which is similar to biological tissues. The fluorescent lifetimes of ICG/DMSO and ICG/ALC are close to the lifetime of ICG *in vivo* (0.60 to 0.84 ns).[27] The phantom size is also close to the size of mice. So the phantoms could be good models of mice. The optical parameters of the background (1% intralipid solution) are set differently at the excitation and emission wavelengths, whereas the same optical parameters were used in our previous papers.[18,19] The voxel size ($0.6 \times 0.6 \times 2$ mm^3) has been improved, and the voxel has smaller sizes in the horizontal directions (0.6×0.6 mm^2) than that in Ref. 19 (1×1 mm^2). The measurement data are normalized by the summation of all the measurement data to eliminate the effects of source power, efficiency of fibers, and filter group and magnification of the detector. The molecular yield and molecular lifetime of the two targets are different, which makes the reconstruction of yield and lifetime difficult, especially when the EED is small. The reconstruction results demonstrate that SGL1PSD is superior to L1PSD and ANOMP in shape recovery, quantification accuracy, and resolution. When the targets are heterogeneous, the targets with large molecular yields will be pronounced in the final reconstructed lifetime map and restrain the reconstruction of the targets with smaller yields. If only the full time gate is employed in the reconstruction of yield *priori*, the ICG/ALC target, which possesses weak yield, will be relatively small [Figs. 4(b), 4(c), 4(f), and 4(g)]. When the EED is small, two reconstruction targets are difficult to separate [Figs. 5(b), 5(c), 5(f), 5(g), 6(b), 6(c), 6(f), and 6(g)]. Although ANOMP performs well when the targets are homogeneous, it cannot improve the reconstruction resolution when they are heterogeneous. The intrinsic causes are the inadequate utilization of the time-resolved data during yield map reconstruction in L1PSD and ANOMP. In addition to the full time strength, the regeneration of the yield map in SGL1PSD introduces the temporal information to provide a refinement. Based on the experiments with different EEDs (only the results of the most typical experiments are presented here), the minimum distances of heterogeneous targets that algorithms can resolve are ~1.5, 5, and 5 mm for SGL1PSD, L1PSD, and ANOMP, respectively. The high resolution and quantification accuracy of SGL1PSD with heterogeneous targets demonstrate that SGL1PSD is promising for the analysis of multiple fluorescent components with distinct lifetimes, targeting at different molecular markers. Because the fluorescent molecular lifetime is sensitive to the physiological factors of the local environment, such as the concentration of tissue oxygenation, glucose and [Ca+], and the pH of tissue fluid, SGL1PSD could be applied to the assessment of a multigene controlling mechanism in a disease progression, the metabolic analysis of multiple tumors, and so on. In addition, both SGL1PSD and ANOMP could provide good resolution when targets are homogeneous. Heterogeneousness makes the reconstruction difficult and brings poor reconstruction resolution. The difference of yield could result in distorted reconstruction size. The target with higher yield will be prominent, whereas the one with lower yield will be restrained. When the yield difference is significant, the reconstruction targets might be even bounded together. When the lifetime values of targets are distinct, it is difficult to keep the reconstruction values accurate. So the lifetime difference will influence the quantification accuracy and contrast. SGL1PSD could still provide good resolution when targets are distinct, whereas ANOMP could not. The reason might be the better data utilization of SGL1PSD, which introduces the time-resolved strategy to yield reconstruction. In contrast, ANOMP only utilizes the full time gate strategy. The results of homogeneous targets are not presented because this study focuses on a heterogeneous target problem. The runtimes of SGL1PSD are slightly longer than those of L1PSD. For Experiment 1, the runtime of ANOMP is much longer than the others. The support set growing is time-consuming for ANOMP. In Experiments 2 and 3, the runtimes of ANOMP are relatively short and meaningless with unstable inner iterations. Therefore, the time cost of SGL1PSD is slightly higher than that of L1PSD, but is much lower than that of ANOMP.

However, for SGL1PSD, when the EEDs of heterogeneous targets are small (Experiments 2 and 3), the reconstruction shapes of targets are slightly distorted. The causes of the distorted shapes might be the huge amount of noise under physical conditions, the severe redundancy of measurement data, and the imperfect approximation of the light propagation model. The optimization of the system parameters and other system settings might reduce the noise. The adjustment of locations of excitation and detection points could increase the effective information. In the future, the forward model of RTE or higher-order approximations of RTE will be adopted. Moreover, the utilization of the measurement data of SGL1PSD might not be optimal. More alternate iterations of time-resolved reconstructions of yield map and inverse lifetime map have also been tested, but the final reconstruction results cannot be improved much, which suggests that four steps in SGL1PSD are enough under the current algorithm settings. The simultaneous reconstruction of yield map and lifetime map based on the time-resolved strategy might be an effective reconstruction method. The time-resolved algorithm adopting the Newton–Raphson scheme with ART to form the inner loops is proposed by Gao et al.[20] The Newton–Raphson scheme adopts Taylor series expansion of the forward function to formulate the outer loop, and ART is employed to obtain the solution in inner loops. The Newton–Raphson scheme turns the nonlinear problem into many linear ones and could reconstruct yield and lifetime at the same time. However, the dimensions of unknown variables in each iteration will be relatively high and the ill-posedness will be severe, which still needs further study.

For FMLT, the system settings (such as the detectors, excitation and detection points, and dark noises), the experimental parameters (such as the position, shape and size of the fluorescence targets, the size of the object, the optical parameters of the object), and the algorithm parameters (such as the size of the discretization grid, the regularization parameter, the stopping criterion, and the initial value) exert a tremendous influence on the reconstruction performance. Automatic selection of the optimal regularization parameters will be our future work.

The selection of regularization parameters might be optimized with the L-curve method, which could be a compromise between the norm of solution and the residual.[28] The U-curve, which is a plot of the sum of the inverse of the regularized solution norm and the corresponding residual norm, might also be used.[28] The regularization parameter at which the U-curve reaches the minimum is possibly the optimum one.

5 Conclusion

The SGL1PSD algorithm is proposed to better utilize the measurement data for TD FMLT. SGL1PSD employs time-resolved strategy in the reconstruction of a molecular yield map, which can provide more accurate *a priori* for lifetime reconstruction. Phantom experiments with heterogeneous targets at different EEDs demonstrate that SGL1PSD can provide high resolution and quantification accuracy for FMLT. SGL1PSD is promising for the analysis of multiple fluorescent components with distinct lifetimes. In the future, the reconstruction shape of targets will be optimized and *in vivo* applications of FMLT will be studied.

Disclosures

All of the authors have no competing interests to disclose.

Acknowledgments

This work was supported by the National Natural Science Foundation of China under Grant Nos. 81227901, 81271617, 61322101, and 61361160418 and the National Major Scientific Instrument and Equipment Development Project under Grant No. 2011YQ030114.

References

1. E. M. Sevick-Muraca et al., "Fluorescence-enhanced, near infrared diagnostic imaging with contrast agents," *Curr. Opin. Chem. Biol.* **6**(5), 642–650 (2002).
2. A. B. Milstein et al., "Fluorescence optical diffusion tomography," *Appl. Opt.* **42**(16), 3081–3094 (2003).
3. V. Ntziachristos et al., "Looking and listening to light: the evolution of whole-body photonic imaging," *Nat. Biotechnol.* **23**(3), 313–320 (2005).
4. J. K. Willmann et al., "Molecular imaging in drug development," *Nat. Rev. Drug Discovery* **7**(7), 591–607 (2008).
5. V. Ntziachristos et al., "Fluorescence molecular tomography resolves protease activity in vivo," *Nat. Med.* **8**(7), 757–761 (2002).
6. J. Lee et al., "Three-dimensional fluorescence enhanced optical tomography using referenced frequency-domain photon migration measurements at emission and excitation wavelengths," *J. Opt. Soc. Am. A* **19**(4), 759–771 (2002).
7. R. Roy et al., "Tomographic fluorescence imaging in tissue phantoms: a novel reconstruction algorithm and imaging geometry," *IEEE Trans. Med. Imaging* **24**(2), 137–154 (2005).
8. V. Y. Soloviev et al., "Fluorescence lifetime imaging by using time-gated data acquisition," *Appl. Opt.* **46**(30), 7384–7391 (2007).
9. S. V. Patwardhan et al., "Quantitative diffuse optical tomography for small animals using an ultrafast gated image intensifier," *J. Biomed. Opt.* **13**(1), 011009 (2008).
10. M. Brambilla et al., "Time-resolved scanning system for double reflectance and transmittance fluorescence imaging of diffusive media," *Rev. Sci. Instrum.* **79**(1), 013103 (2008).
11. M. A. O'Leary et al., "Fluorescence lifetime imaging in turbid media," *Opt. Lett.* **21**(2), 158–160 (1996).
12. J. McGinty et al., "*In vivo* fluorescence lifetime tomography of a FRET probe expressed in mouse," *Biomed. Opt. Express* **2**(7), 1907–1917 (2011).
13. S. S. Hou et al., "Tomographic lifetime imaging using combined early- and late-arriving photons," *Opt. Lett.* **39**(5), 1165–1168 (2014).
14. W. L. Rice et al., "Resolution below the point spread function for diffuse optical imaging using fluorescence lifetime multiplexing," *Opt. Lett.* **38**(12), 2038–2040 (2013).
15. R. E. Nothdurft et al., "*In vivo* fluorescence lifetime tomography," *J. Biomed. Opt.* **14**(2), 024004 (2009).
16. L. Zhang et al., "Three-dimensional scheme for time-domain fluorescence molecular tomography based on Laplace transforms with noise-robust factors," *Opt. Express* **16**(10), 7214–7223 (2008).
17. F. Gao et al., "Simultaneous fluorescence yield and lifetime tomography from time-resolved transmittances of small-animal-sized phantom," *Appl. Opt.* **49**(16), 3163–3172 (2010).
18. C. Cai et al., "Direct reconstruction method for time-domain fluorescence molecular lifetime tomography," *Opt. Lett.* **40**(17), 4038–4041 (2015).
19. C. Cai et al., "Nonlinear greedy sparsity-constrained algorithm for direct reconstruction of fluorescence molecular lifetime tomography," *Biomed. Opt. Express* **7**(4), 1210–1226 (2016).
20. F. Gao et al., "A self-normalized, full time-resolved method for fluorescence diffuse optical tomography," *Opt. Express* **16**(17), 13104–13121 (2008).
21. C. Qin et al., "Galerkin-based meshless methods for photon transport in the biological tissue," *Opt. Express* **16**(25), 20317–20333 (2008).
22. B. Zhang et al., "Early-photon fluorescence tomography of a heterogeneous mouse model with the telegraph equation," *Appl. Opt.* **50**(28), 5397–5407 (2011).
23. S. R. Arridge, "Optical tomography in medical imaging," *Inverse Probl.* **15**(2), R41 (1999).
24. A. Neumaier, "Solving ill-conditioned and singular linear systems: a tutorial on regularization," *SIAM Rev.* **40**(3), 636–666 (1998).
25. H. Lee et al., "Fluorescence lifetime properties of near-infrared cyanine dyes in relation to their structures," *J. Photochem. Photobiol., A* **200**(2), 438–444 (2008).
26. H. Pu et al., "Resolving fluorophores by unmixing multispectral fluorescence tomography with independent component analysis," *Phys. Med. Biol.* **59**(17), 5025–5042 (2014).
27. M. Y. Berezin et al., "Long fluorescence lifetime molecular probes based on near infrared pyrrolopyrrole cyanine fluorophores for *in vivo* imaging," *Biophys. J.* **97**(9), L22–L24 (2009).
28. J. Chamorro-Servent et al., "Feasibility of U-curve method to select the regularization parameter for fluorescence diffuse optical tomography in phantom and small animal studies," *Opt. Express* **19**(12), 11490–11506 (2011).

Chuangjian Cai received his bachelor's degree in biomedical engineering from Tsinghua University, Beijing, China, in 2015. Currently, he is a PhD student in the Department of Biomedical Engineering, Tsinghua University. His research interest is FMT for small animal imaging.

Wenjuan Cai received her bachelor's degree in biomedical engineering from Huazhong University of Science and Technology, Wuhan, China, in 2014. Currently, she is an MS student in the Department of Biomedical Engineering, Tsinghua University, Beijing, China. Her research interests focus on *in vivo* fluorescence imaging and FMLT.

Jiaju Cheng received his bachelor's degree in biomedical engineering from Tsinghua University, Beijing, China, in 2016. Currently, he is a PhD student in the Department of Biomedical Engineering, Tsinghua University. His research interest is FMT for small animal imaging.

Yuxuan Yang received her bachelor's degree in electrical engineering from North China Electric Power University, Baoding, China, in 2016. Currently, she is an MS student in the Department of Biomedical Engineering, Tsinghua University. Her research interest is FMT for small animal imaging.

Jianwen Luo is a professor at Tsinghua University. He was enrolled in the Thousand Young Talents Program of China in 2012, received the Excellent Young Scientists Fund from the National Natural Science Foundation of China in 2013, and was funded by the Young Scientist Project of National Key R&D Program of China in 2016. His research interest is biomedical imaging, including ultrasound imaging, and fluorescence molecular imaging.